J. Fluid Mech. (2012), *vol.* 700, *pp.* 304–328.
doi:10.1017/jfm.2012.133

Nonlinear liquid sloshing in a square tank subjected to obliquely horizontal excitation

Takashi Ikeda[1]†, Raouf A. Ibrahim[2], Yuji Harata[1] and Tasuku Kuriyama[3]

[1] Department of Mechanical Systems Engineering, Faculty of Engineering, Hiroshima University, 1-4-1, Kagamiyama, Higashi-Hiroshima, Hiroshima 739-8527, Japan

[2] Department of Mechanical Engineering, Wayne State University, Detroit, MI 48202, USA

[3] Terumo Corporation, 2-44-1, Hatagaya, Shibuya-ku, Tokyo 151-0072, Japan

(Received 5 October 2011; revised 14 February 2012; accepted 6 March 2012; first published online 1 May 2012)

Nonlinear responses of surface waves in rigid square and nearly square tanks partially filled with liquid subjected to obliquely horizontal, sinusoidal excitation are investigated theoretically and experimentally. Two predominant modes of sloshing are significantly coupled nonlinearly because their natural frequencies are nearly identical resulting in 1:1 internal resonance. Therefore, if only one of these modes is directly excited, the other mode is indirectly excited due to the nonlinear coupling. In the nonlinear theoretical analysis, the modal equations of motion are derived for the two predominant sloshing modes as well as five higher sloshing modes. The linear viscous terms are incorporated in order to consider the damping effect of sloshing. The expressions for the frequency response curves are determined using van der Pol's method. The influences of the excitation direction and the aspect ratio of the tank cross-section on the frequency response curves are numerically examined. Planar and swirl motions of sloshing, and Hopf bifurcations followed by amplitude modulated motions including chaotic motions, are predicted when the excitation frequency is close to one of the natural frequencies of the two predominant sloshing modes. Lyapunov exponents are calculated and reveal the excitation frequency range over which liquid chaotic motions occur. In addition, bifurcation sets are shown to clarify the influences of the parameters on the change in the structural stability. The theoretically predicted results are in good agreement with the measured data, thus the theoretical analysis was experimentally validated.

Key words: bifurcation, nonlinear dynamical systems, waves/free-surface flows

1. Introduction

There are many mechanical systems that include liquid tanks such as large liquid storage tanks, liquefied natural gas tankers and liquid fuel rockets (Ibrahim 2005; Faltinsen & Timokha 2009). Liquid surface wave motion in these tanks is referred to as sloshing. Large-amplitude sloshing exerts excessive hydrodynamic loads on the tank walls and there is a higher risk of both damage to the tank and overspill of the liquid. For example, sloshing sometimes causes severe damage to floating

† Email address for correspondence: tikeda@hiroshima-u.ac.jp

roofs and sidewalls of large oil storage tanks. Furthermore, earthquakes may cause violent, chaotic sloshing in spent-fuel storage pools of nuclear power plants resulting in contaminated water being spilled. This is because the frequency spectrum of earthquakes contains a wide range of excitation frequencies. Violent sloshing occurs if one of these frequencies is near one of the natural frequencies of sloshing modes. The behaviour of sloshing under random excitation as observed during earthquakes is extremely complicated, thus it is important to first study sloshing under sinusoidal excitation as a fundamental examination of liquid sloshing dynamics.

Two-dimensional nonlinear sloshing in rectangular tanks, subjected to horizontal, harmonic excitation along the tank length, has been investigated (see e.g. Hayama, Aruga & Watanabe 1983; Hill 2003). Feng (1997) experimentally observed the transition from steady-state standing waves to non-steady travelling waves and theoretically proved that the energy exchange between two neighbouring modes resulted in amplitude-modulated motions (AMMs) even if only one of the modes was directly excited (Feng 1998). Three-dimensional nonlinear sloshing in a partially filled rigid rectangular tank, subjected to a combination of pitch, horizontal and vertical excitation, was investigated by Kimura, Takahara & Ogura (1996). They derived modal equations of motion, calculated time histories and compared them with experimental data and later obtained frequency response curves (Takahara & Kimura 2002). The aspect ratio of the tank cross-section was adjusted to include the case where the natural frequencies of the two predominant sloshing modes were equal in both papers. Faltinsen *et al.* (2000) derived the multidimensional modal system for nonlinear sloshing in a rectangular tank with finite water depth and showed that time-dependent coordinates of the liquid elevation and velocity potential were nonlinearly coupled. Several nonlinear studies were conducted dealing with liquid sloshing in circular cylindrical tanks subjected to horizontal excitation (Hutton 1963; Abramson 1966; Miles 1984; Funakoshi & Inoue 1988). Planar and swirl motions, and the transitions from planar waves to chaotic motions were theoretically examined and compared with the numerical simulation results and the experimental data. In circular cylindrical tanks, the predominant modes (1, 0) and (0, 1) have an identical natural frequency and are degenerated, though not fixed to the tank. Thus when subjected to horizontal excitation perpendicular to the nodal diameter of the (1, 0) mode, only this mode is excited, and the excitation direction does not affect the dynamic behaviour of sloshing. Sloshing dynamics in square tanks at first appear to be similar to those in circular cylindrical tanks; however, depending on the excitation direction, both (1, 0) and (0, 1) modes may be directly excited because they are fixed to the tank. Accordingly, more complicated behaviours of sloshing are expected to be observed in square and nearly square tanks. The influence of the excitation direction on liquid sloshing in square and nearly square tanks is one of the key elements that will be focused on in the present paper because it has not been thoroughly examined in the fluid dynamics literature.

Faltinsen, Rognebakke & Timokha (2003, 2005, 2006*a*,*b*) conducted a series of investigations of nonlinear sloshing in a square-base basin tank, subjected to surge/sway/roll/pitch harmonic excitation. Faltinsen *et al.* (2003) extended the two-dimensional modelling of Faltinsen *et al.* (2000) to apply to three-dimensional nonlinear sloshing analysis and showed the theoretical frequency response curves. Two primary modes were assumed to be dominant and three wave patterns were observed: 'planar'/'diagonal', 'swirling' and 'square'-like resonant standing waves. It was concluded that higher sloshing modes in steady-state and transient flows influence three-dimensional sloshing dynamics. However, because of a discrepancy caused by nonlinear amplification of higher modes due to internal resonance, Faltinsen

et al. (2005) improved the accuracy of the theoretical analysis. Faltinsen *et al.* (2006*a*) found that small perturbations of the aspect ratio of the tank cross-section significantly influenced the frequency response curves. Further investigation on the transition from steady-state waves to 'swirling' waves and 'beating', including a discussion on chaotic waves, was performed by Faltinsen *et al.* (2006*b*). Although the damping of higher modes was found to be difficult to model, and 'adaptive modal modelling' was proposed as a possible means of including the linear damping effect, the frequency response curves do not reflect the influence of the damping. Royon-Lebeaud, Hopfinger & Cartellier (2007) experimentally investigated sloshing behaviour in a square tank subjected to horizontal harmonic excitation along its length. They observed planar, swirling, and breaking waves as well as chaotic sloshing depending on the excitation frequency and excitation amplitude. Yoshimatsu & Funakoshi (2001) conducted detailed analysis for a square tank subjected to horizontal excitation and explored the influence of the excitation direction at various angles. They found that swirl motion appeared and Hopf bifurcation occurred; however, only two sloshing modes were considered in the nonlinear analysis. Because the response curves were shown in terms of vibration energy generated by the two modes, it was difficult to distinguish the response of each sloshing mode. In addition, the validity of the theoretical results was not experimentally confirmed. Ikeda & Ibrahim (2008) examined the same system (Yoshimatsu & Funakoshi 2001) and used potential theory to derive the modal equations of motion, taking into consideration the nonlinearity and damping effect of sloshing. Although they showed the theoretical frequency response curves, there was a discrepancy between them and the experimental data, possibly because additional higher sloshing modes were not considered in the theoretical analysis.

The present study investigates the nonlinear responses of sloshing in a rigid square tank subjected to obliquely horizontal, harmonic excitation. The present work improves the accuracy of the theoretical analysis which was conducted by Ikeda & Ibrahim (2008). Galerkin's method is employed to derive the modal equations of motion for seven sloshing modes: predominant modes (1, 0) and (0, 1), higher modes (2, 0), (0, 2), (3, 0) and (0, 3), and the additional higher mode (1, 1) which had not been considered previously. Van der Pol's method (Stoker 1950) is applied to the modal equations of motion to determine the frequency response curves for sloshing. Because the theoretical analysis is performed taking into account the damping effects of sloshing, the response curves are superior for revealing the behaviours of nonlinear sloshing such as planar and swirl motions and AMMs including chaotic motions. It is also found that higher sloshing mode (1, 1) plays a significant role in improving the accuracy of the frequency response curves. In real systems, the direction of the external horizontal excitation is arbitrary in relation to the liquid tank and thus the influence of the excitation direction is thoroughly investigated by showing response curves and calculating bifurcation sets. Furthermore perfectly square tanks do not exist in reality due to manufacturing errors, thus the influence of the aspect ratio of the tank cross-section is also examined. Experiments were conducted to confirm the validity of the theoretical analysis.

2. Theoretical analysis

2.1. *Equations of motion*

Figure 1 shows a rigid, nearly square tank with a cross-section area of width times breadth $l \times w$, partially filled with liquid to the level h. The Cartesian coordinate

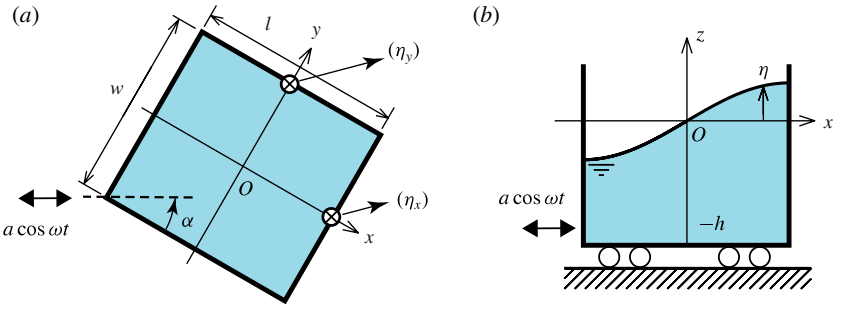

FIGURE 1. (Colour online available at journals.cambridge.org/flm) Theoretical model: (*a*) top view, (*b*) side view.

system, *O*-*xyz*, is fixed to the tank, where the *xy*-plane coincides with the undisturbed liquid free surface. The tank is subjected to horizontal excitation $a\cos\omega t$, where a is excitation amplitude, ω excitation frequency, t time, and the direction of excitation deviates from the x-axis of the tank by angle α. The translation (x_0, y_0) of the tank motion can be given by

$$x_0 = a\cos\alpha\cos\omega t, \quad y_0 = a\sin\alpha\cos\omega t. \tag{2.1}$$

When α does not equal zero, the tank is simultaneously subjected to two kinds of horizontal excitation x_0 and y_0 in the x- and y-directions, respectively. The liquid elevation at position (x, y) is designated by $\eta(x, y, t)$. In the theoretical analysis, the liquid is assumed to be a perfect fluid; hence the velocity potential $\phi(x, y, z, t)$ can be introduced in order to represent the liquid motion relative to the tank. P is the fluid pressure, and ρ is the fluid density. The damping effect of sloshing will be considered by adding the viscous damping terms to the modal equations for sloshing. The following dimensionless quantities are introduced:

$$a' = a/l, \quad h' = h/l, \quad w' = w/l, \quad x_0' = x_0/l, \quad y_0' = y_0/l, \quad z' = z/l, \quad \eta' = \eta/l, \tag{2.2}$$

$$\phi' = \phi/(l^2 p_{10}), \quad P' = P/(\rho l^2 p_{10}^2), \quad \lambda_{ij}' = \lambda_{ij} l, \tag{2.3}$$

$$\omega' = \omega/p_{10}, \quad p_{ij}' = p_{ij}/p_{10}, \quad t' = p_{10} t, \tag{2.4}$$

where

$$\lambda_{ij} = \pi\sqrt{(i/l)^2 + (j/w)^2}, \quad p_{ij} = \sqrt{g\lambda_{ij}\tanh(\lambda_{ij} h)} \tag{2.5}$$

where g is the acceleration due to gravity, and p_{ij} represents the natural frequency of the (i, j) sloshing mode. Figures 2(*a*) and 2(*b*) show the shapes of (1, 0) and (0, 1) sloshing modes, respectively. The nodal lines of these modes coincide with the y- and x-axes, respectively. It should be noted that all primes in (2.2) to (2.4) will hereafter be omitted for simplicity although the quantities are still dimensionless in the theoretical analysis and results.

Laplace's equation and Euler's energy equation for the fluid motion are expressed in dimensionless form, respectively, as

$$\frac{\partial^2\phi}{\partial x^2} + \frac{\partial^2\phi}{\partial y^2} + \frac{\partial^2\phi}{\partial z^2} = 0, \tag{2.6}$$

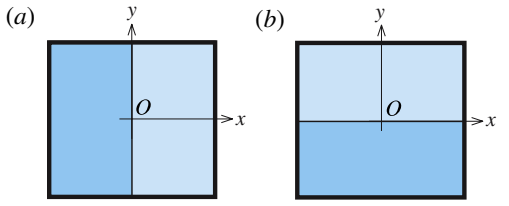

FIGURE 2. (Colour online) Mode shapes: (*a*) (1, 0) mode; (*b*) (0, 1) mode.

$$\frac{\partial \phi}{\partial t} + \frac{1}{2}\left[\left(\frac{\partial \phi}{\partial x}\right)^2 + \left(\frac{\partial \phi}{\partial y}\right)^2 + \left(\frac{\partial \phi}{\partial z}\right)^2\right] + \frac{z}{\psi_{10}} + P = -\ddot{x}_0 x - \ddot{y}_0 y, \tag{2.7}$$

where $\psi_{10} = \lambda_{10}\tanh(\lambda_{10}h)$. The boundary conditions for the fluid velocity at the tank walls and bottom are given as

$$\left.\begin{aligned} &\frac{\partial \phi}{\partial x} = 0 \quad (\text{at } x = \pm 1/2), \qquad \frac{\partial \phi}{\partial y} = 0 \quad (\text{at } y = \pm w/2), \\ &\frac{\partial \phi}{\partial z} = 0 \quad (\text{at } z = -h). \end{aligned}\right\} \tag{2.8}$$

In addition, the kinematic boundary condition at the liquid free surface is given as

$$\frac{\partial \phi}{\partial z} = \frac{\partial \eta}{\partial t} + \frac{\partial \phi}{\partial x}\frac{\partial \eta}{\partial x} + \frac{\partial \phi}{\partial y}\frac{\partial \eta}{\partial y} \quad (\text{at } z = \eta). \tag{2.9}$$

Because $P = 0$ at the liquid free surface, the boundary condition for (2.7) is obtained as

$$\frac{\partial \phi}{\partial t} + \frac{1}{2}\left[\left(\frac{\partial \phi}{\partial x}\right)^2 + \left(\frac{\partial \phi}{\partial y}\right)^2 + \left(\frac{\partial \phi}{\partial z}\right)^2\right] + \frac{z}{\psi_{10}} = -\ddot{x}_0 x - \ddot{y}_0 y \quad (\text{at } z = \eta). \tag{2.10}$$

Equations (2.6) to (2.10) constitute the boundary value problem for liquid sloshing in square and nearly square tanks. The next section will be devoted to developing the modal equations of motion for the two predominant sloshing modes in addition to five higher modes.

2.2. *Modal equations of motion for sloshing*

Galerkin's method is used to search for the solutions of the forced oscillations for the nonlinear system. Here ϕ and η are assumed in terms of the eigenfunctions which can be obtained from the corresponding linear system, as follows:

$$\phi(x, y, z, t) = \sum_{i=0}^{\infty}\sum_{j=0}^{\infty} a_{ij}(t)U_{ij}(x, y)\cosh\{\lambda_{ij}(z + h)\}/\cosh(\lambda_{ij}h), \tag{2.11a}$$

$$\eta(x, y, t) = \sum_{i=0}^{\infty}\sum_{j=0}^{\infty} b_{ij}(t)U_{ij}(x, y), \tag{2.11b}$$

where $U_{ij}(x, y)$ represent eigenfunctions and are expressed by

$$U_{ij}(x,y) = \begin{cases} \sin(\lambda_{i0}x)\sin(\lambda_{0j}y) & (i=2m+1, j=2n+1), \\ \sin(\lambda_{i0}x)\cos(\lambda_{0j}y) & (i=2m+1, j=2n), \\ \cos(\lambda_{i0}x)\sin(\lambda_{0j}y) & (i=2m, j=2n+1), \\ \cos(\lambda_{i0}x)\cos(\lambda_{0j}y) & (i=2m, j=2n), \end{cases} \tag{2.12}$$

where m and $n = 0, 1, 2, \ldots$. Note that λ_{ij} in (2.12) represent dimensionless quantities given by (2.3) and (2.5); $a_{ij}(t)$ and $b_{ij}(t)$ in (2.11*a*,*b*) are unknown functions of time. The coordinates x and y on the right-hand sides of (2.7) and (2.10) can be expanded in terms of the eigenfunctions of (2.12) as follows:

$$x = \sum_{i=1}^{\infty}[r_{i0}U_{i0}(x,y)], \quad y = \sum_{j=1}^{\infty}[r_{0j}U_{0j}(x,y)], \tag{2.13}$$

where the coefficients r_{i0} and r_{0j} are given as

$$\left.\begin{aligned} r_{i0} &= \begin{cases} 2\displaystyle\int_{-1/2}^{1/2} x\sin(\lambda_{i0}x)\,\mathrm{d}x = (-1)^{(i-1)/2}\frac{4}{i^2\pi^2} & (i=1,3,5,\ldots) \\ 2\displaystyle\int_{-1/2}^{1/2} x\cos(\lambda_{i0}x)\,\mathrm{d}x = 0 & (i=0,2,4,\ldots), \end{cases} \\ r_{0j} &= \begin{cases} \dfrac{2}{w}\displaystyle\int_{-w/2}^{w/2} y\sin(\lambda_{0j}y)\,\mathrm{d}y = (-1)^{(j-1)/2}\frac{4w}{i^2\pi^2} & (j=1,3,5,\ldots) \\ \dfrac{2}{w}\displaystyle\int_{-w/2}^{w/2} y\cos(\lambda_{0j}y)\,\mathrm{d}y = 0 & (j=0,2,4,\ldots). \end{cases} \end{aligned}\right\} \tag{2.14}$$

ε is introduced as a bookkeeping parameter to determine the approximate solutions when sloshing modes (1, 0) and (0, 1) predominantly appear. Therefore, the orders of $a_{ij}(t)$ and $b_{ij}(t)$ in (2.11*a*,*b*), x_0 and y_0 in (2.10), and the system parameters, ζ_{ij} and a, are assumed as follows:

$$a_{10}, a_{01}, b_{10}, \zeta_{ij} \approx O(\varepsilon^{1/3}), \tag{2.15a}$$

$$a_{20}, a_{02}, a_{30}, a_{03}, a_{11}, b_{20}, b_{02}, b_{30}, b_{03}, b_{11} \approx O(\varepsilon^{2/3}), \tag{2.15b}$$

$$a_{i0}, a_{0j}, a_{ij}, b_{i0}, b_{0j}, b_{ij}, x_0, y_0, a \approx O(\varepsilon^{3/3}) \quad (i \geqslant 4, j \geqslant 4). \tag{2.15c}$$

Equations (2.15) partially follow Moiseev's ordering (Moiseev 1958) where (1, 0) and (0, 1) modes are of $O(\varepsilon^{1/3})$, (2, 0), (1, 1) and (0, 2) modes are of $O(\varepsilon^{2/3})$, and (3, 0), (2, 1), (1, 2) and (0, 3) are of $O(\varepsilon^{3/3})$. However, the orders of (3, 0) and (0, 3) modes are amplified to $O(\varepsilon^{2/3})$, and modes (1, 2) and (2, 1) are not considered. Furthermore, the damping ratios ζ_{ij} are assumed to be of $O(\varepsilon^{1/3})$ so that modal equations for all modes include the damping effect. This ordering is preferred to obtain accurate theoretical results that agree with the corresponding experimental data as shown by Ikeda & Nakagawa (1997).

Equations (2.9) and (2.10) are expanded into Taylor's series about $\eta = 0$, and (2.11*a*,*b*) are substituted into the two resulting equations. By equating the coefficients of $\sin(\lambda_{10}x)$, $\sin(\lambda_{01}y)$, $\cos(\lambda_{20}x)$, $\cos(\lambda_{02}y)$, $\sin(\lambda_{30}x)$, $\sin(\lambda_{03}y)$ and $\sin(\lambda_{10}x)\sin(\lambda_{01}y)$ on both sides of these two equations within the accuracy of $O(\varepsilon)$, and eliminating a_{ij} from the resulting equations, one can obtain the modal equations of motion for

sloshing:

$$\left.\begin{aligned}
&\ddot{b}_{10}+2\zeta_{10}\dot{b}_{10}+b_{10}+H_1(b_{10},b_{01},b_{20},b_{11})=\psi_{10}r_{10}a\omega^2\cos\alpha\cos\omega t,\\
&\ddot{b}_{01}+2\zeta_{01}\omega_{01}\dot{b}_{01}+\omega_{01}^2b_{01}+H_2(b_{10},b_{01},b_{02},b_{11})=\psi_{01}r_{01}a\omega^2\sin\alpha\cos\omega t,\\
&\ddot{b}_{20}+2\zeta_{20}\omega_{20}\dot{b}_{20}+\omega_{20}^2b_{20}+H_3(b_{10},b_{01},b_{30})=0,\\
&\ddot{b}_{02}+2\zeta_{02}\omega_{02}\dot{b}_{02}+\omega_{02}^2b_{02}+H_4(b_{10},b_{01},b_{03})=0,\\
&\ddot{b}_{30}+2\zeta_{30}\omega_{30}\dot{b}_{30}+\omega_{30}^2b_{30}+H_5(b_{10},b_{01},b_{20})=\psi_{30}r_{30}a\omega^2\cos\alpha\cos\omega t,\\
&\ddot{b}_{03}+2\zeta_{03}\omega_{03}\dot{b}_{03}+\omega_{03}^2b_{03}+H_6(b_{10},b_{01},b_{02})=\psi_{03}r_{03}a\omega^2\sin\alpha\cos\omega t,\\
&\ddot{b}_{11}+2\zeta_{11}\omega_{11}\dot{b}_{11}+\omega_{11}^2b_{11}+H_7(b_{10},b_{01})=0,
\end{aligned}\right\}\tag{2.16}$$

where $\omega_{ij}^2=\psi_{ij}/\psi_{10}$ and $\psi_{ij}=\lambda_{ij}\tanh(\lambda_{ij}h)$. Note that linear viscous damping terms $2\zeta_{ij}\omega_{ij}\dot{b}_{ij}$ are incorporated in (2.16) to consider the damping effect of sloshing. If Moiseev's ordering is used, the damping terms are not included in the modal equations for (3, 0) and (0, 3) modes. The nonlinear terms H_m $(m=1,2,\ldots,7)$ in (2.16) are given in the Appendix. Because the nonlinear terms of b_{10} and b_{01} are included in H_1 and H_2, the predominant modes (1, 0) and (0, 1) are nonlinearly coupled and form an autoparametric system. Higher mode (1, 1) is nonlinearly coupled with both predominant modes and is thus expected to play a significant role in nonlinear sloshing dynamics. Higher modes (2, 0) and (0, 2) are nonlinearly coupled with (1, 0) and (0, 1) modes, respectively. Note that higher modes (3, 0) and (0, 3) are nonlinearly coupled with (2, 0) and (0, 2) modes, respectively, but do not directly influence the predominant modes. Additionally, higher modes (1, 2) and (2, 1) could be considered, but are also not nonlinearly coupled with the two predominant modes and have thus been omitted in the present analysis.

2.3. *Frequency response curves*

Van der Pol's method (Stoker 1950) is employed to determine the frequency response curves for liquid sloshing. According to the fast Fourier transform (FFT) results of the time histories obtained by numerically integrating (2.16), the solution of the harmonic oscillation near the excitation frequency $\omega\cong p_{10}\cong p_{01}$ can be assumed in the following expression:

$$\left.\begin{aligned}
b_{10}&=u_1\cos\omega t-v_1\sin\omega t+e_1\cos3\omega t-f_1\sin3\omega t,\\
b_{01}&=u_2\cos\omega t-v_2\sin\omega t+e_2\cos3\omega t-f_2\sin3\omega t,\\
b_{20}&=e_3\cos2\omega t-f_3\sin2\omega t+R_{20},\\
b_{02}&=e_4\cos2\omega t-f_4\sin2\omega t+R_{02},\\
b_{30}&=e_5\cos\omega t-f_5\sin\omega t+e_6\cos3\omega t-f_6\sin3\omega t,\\
b_{03}&=e_7\cos\omega t-f_7\sin\omega t+e_8\cos3\omega t-f_8\sin3\omega t,\\
b_{11}&=e_9\cos2\omega t-f_9\sin2\omega t+R_{11}.
\end{aligned}\right\}\tag{2.17}$$

The terms of the frequency 2ω are included in b_{11} of (2.17) because they become significantly large for low liquid levels. The amplitudes and phase angles of (1, 0) and (0, 1) modes for the primary harmonic oscillation can be given by

$$A_{10}=\sqrt{u_1^2+v_1^2},\quad A_{01}=\sqrt{u_2^2+v_2^2},\quad \phi_{10}=\tan^{-1}(v_1/u_1),\quad \phi_{01}=\tan^{-1}(v_2/u_2).\tag{2.18}$$

The amplitudes u_i, v_i, e_j and f_j $(i=1,2;\ j=1,2,\ldots,9)$ and the constant terms R_{20}, R_{02} and R_{11} in (2.17) are assumed to vary slowly over time and hence they are

assumed to have the following orders:

$$\left.\begin{array}{ll} u_i,\, v_i,\, \zeta_{ij} = O(\varepsilon^{1/3}), & e_j, f_j, R_{20}, R_{02}, R_{11} = O(\varepsilon^{2/3}), \\ \dot{u}_i,\, \dot{v}_i = O(\varepsilon^{3/3}), & \dot{e}_j, \dot{f}_j, \dot{R}_{20}, \dot{R}_{02}, \dot{R}_{11} = O(\varepsilon^{4/3}), \\ \ddot{u}_i,\, \ddot{v}_i = O(\varepsilon^{5/3}), & \ddot{e}_j, \ddot{f}_j, \ddot{R}_{20}, \ddot{R}_{02}, \ddot{R}_{11} = O(\varepsilon^{2}). \end{array}\right\} \tag{2.19}$$

Substituting (2.17) into (2.16), and equating the coefficients of the terms of the frequencies ω, 2ω, 3ω and the constant terms within the accuracy of $O(\varepsilon)$ according to the orders listed in (2.19), gives

$$\left.\begin{array}{l} \dot{u}_1 = G_1(u_i, v_i, e_j, f_j, R_{20}, R_{11}), \\ \dot{v}_1 = G_2(u_i, v_i, e_j, f_j, R_{20}, R_{11}), \\ \dot{u}_2 = G_3(u_i, v_i, e_j, f_j, R_{02}, R_{11}), \\ \dot{v}_2 = G_4(u_i, v_i, e_j, f_j, R_{02}, R_{11}), \\ G_k(u_i, v_i, e_j, f_j, R_{20}, R_{02}, R_{11}) = 0, \end{array}\right\} \tag{2.20}$$

where G_n $(n = 1, 2, \ldots, 25)$ represent the nonlinear terms consisting of the variables shown in the parentheses. G_k $(k = 5, 6, \ldots, 25)$ are linear polynomials in terms of e_j, f_j, R_{20}, R_{02} and R_{11}. The complete expressions of G_n are omitted here. The analytical steady-state solutions of (2.20) can be numerically calculated by applying Brent's method for the nonlinear, simultaneous equations obtained by setting $\dot{u}_i$ and $\dot{v}_i$ in (2.20) to zero. In addition, a stability analysis for the steady-state solutions can be conducted by introducing small deviations from them, following the same procedure as Ikeda & Nakagawa (1997). Theoretical response curves can then be plotted using (2.18) to estimate the response amplitudes and phase angles.

3. Numerical results

In the following numerical calculations, the values of the system parameters are given in such a way that the natural frequencies of (1, 0) and (0, 1) modes are equal or nearly equal to the excitation frequency ω, i.e. $p_{10} \cong p_{01} \cong \omega \cong 1$. This condition implies 1:1 internal resonance as well as external primary resonance.

3.1. *Frequency response curves*

Figure 3(*a*) shows the amplitude–frequency responses for A_{10} and A_{01} of (1, 0) and (0, 1) sloshing modes when the excitation direction is parallel to the tank length. The values of the system parameters are $h = 0.6$, $w = 1.0$, $\zeta_{ij} = 0.013$, $a = 0.0075$, and $\alpha = 0°$ and the tank is square so the natural frequencies of (1, 0) and (0, 1) modes are equal to 1.0. The solid and broken lines represent the stable and unstable steady-state solutions, respectively. The symbol '•' represents the constant amplitude of the frequency component ω which is calculated using the FFT analysis of the time histories obtained from the numerical simulation of (2.16). The vertical thin line represents the magnitude of the modulated amplitudes of the AMMs obtained from the numerical simulation. It is found that the theoretical response curves are in good agreement with the simulation results. When $\alpha = 0°$, only (1, 0) mode is directly excited and branch $A_1Q_1P_1C_1D_1$ is typical of a soft nonlinear Duffing oscillator similar to rectangular tank results (Hayama *et al.* 1983; Faltinsen *et al.* 2000). Branch $A_2Q_2P_2C_2D_2$ of (0, 1) mode, which is stable with zero amplitude for rectangular tanks, consists of both stable and unstable solutions. Furthermore, new branch $B_2E_2F_2I_2C_2$ emerges and the corresponding branch $B_1E_1F_1I_1C_1$ appears, and branches

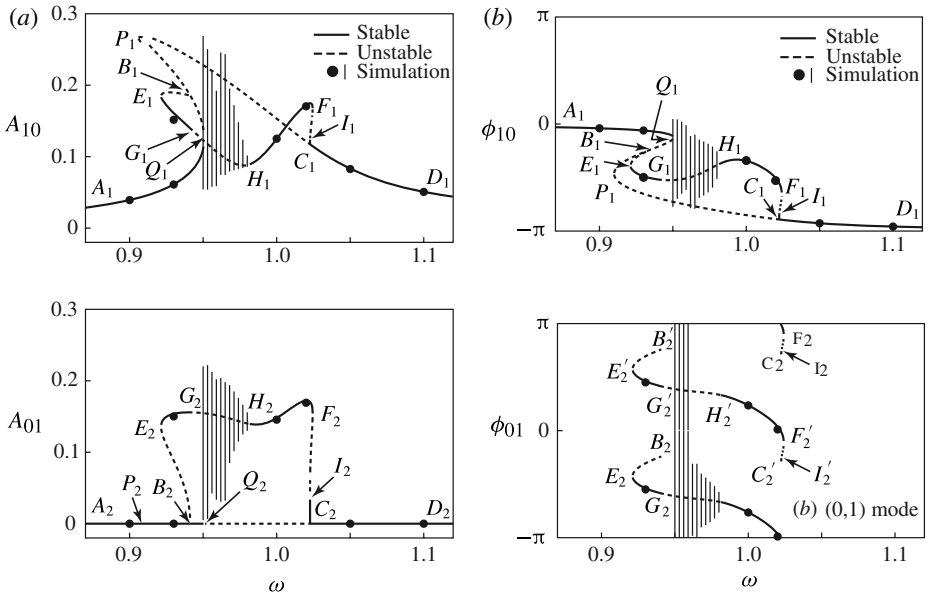

FIGURE 3. Frequency response curves of sloshing modes (1, 0) and (0, 1) for $h = 0.6$, $w = 1.0$, $\zeta_{ij} = 0.013$, $a = 0.0075$ and $\alpha = 0°$: (*a*) modal amplitudes A_{10} and A_{01}; (*b*) modal phase angles ϕ_{10} and ϕ_{01}.

P_iC_i $(i = 1, 2)$ are unstable. This is because the (0, 1) mode is also simultaneously excited due to the nonlinear coupling. For the purpose of this paper, this effect will be known as the 'autoparametric interaction', and appears over the excitation frequency range B_iC_i. Further investigating branches $B_iE_iF_iC_i$, it is found that branches E_iG_i, H_iF_i and I_iC_i are stable and branches G_iH_i and F_iI_i are unstable. When the initial conditions are chosen from the steady-state solutions of unstable branches G_iH_i in the numerical simulations, AMMs are observed. Therefore, it is found that points G_i and H_i are Hopf bifurcation points. There is a small gap near points G_i where AMMs do not appear because the amplitudes jump to the stable branches A_iQ_i. Furthermore, it should be noted that when the excitation frequency increases, stable branch A_2Q_2 overlaps unstable branch $Q_2P_2C_2$, and a jump phenomenon occurs at point Q_2, not at pitchfork bifurcation point B_2 as reported by Ikeda (2003). Figure 3(*b*) shows the frequency response curves for phase angles ϕ_{10} and ϕ_{01} of (1, 0) and (0, 1) modes, which correspond to the amplitude curves of figure 3(*a*). The symbol '•' represents the constant phase angle of the frequency component ω which is calculated by an FFT analysis of the time histories. Branch $A_1Q_1P_1C_1D_1$ is similar to the phase response curve of the Duffing system. The corresponding branch does not exist for ϕ_{01}, because the amplitude of mode (0, 1) is zero and hence its phase angle cannot be defined. Branch $B_1E_1F_1I_1C_1$ appears in ϕ_{10}, whereas an additional branch $B_2'E_2'F_2'I_2'C_2'$ also appears at a distance of π from branch $B_2E_2F_2I_2C_2$ in ϕ_{01} in figure 3(*b*). The vertical thin line represents the magnitude of the modulated phase angles of the AMMs. They are plotted only for branches G_iH_i. It is found that the theoretical response curves are also in good agreement with the simulation results.

In order to thoroughly understand the sloshing behaviour shown in figures 3(*a*) and 3(*b*), time histories, orbits of the liquid surface (Lissajous curves), and Poincaré maps are shown in figure 4. Here η_x and η_y represent the liquid surface elevations

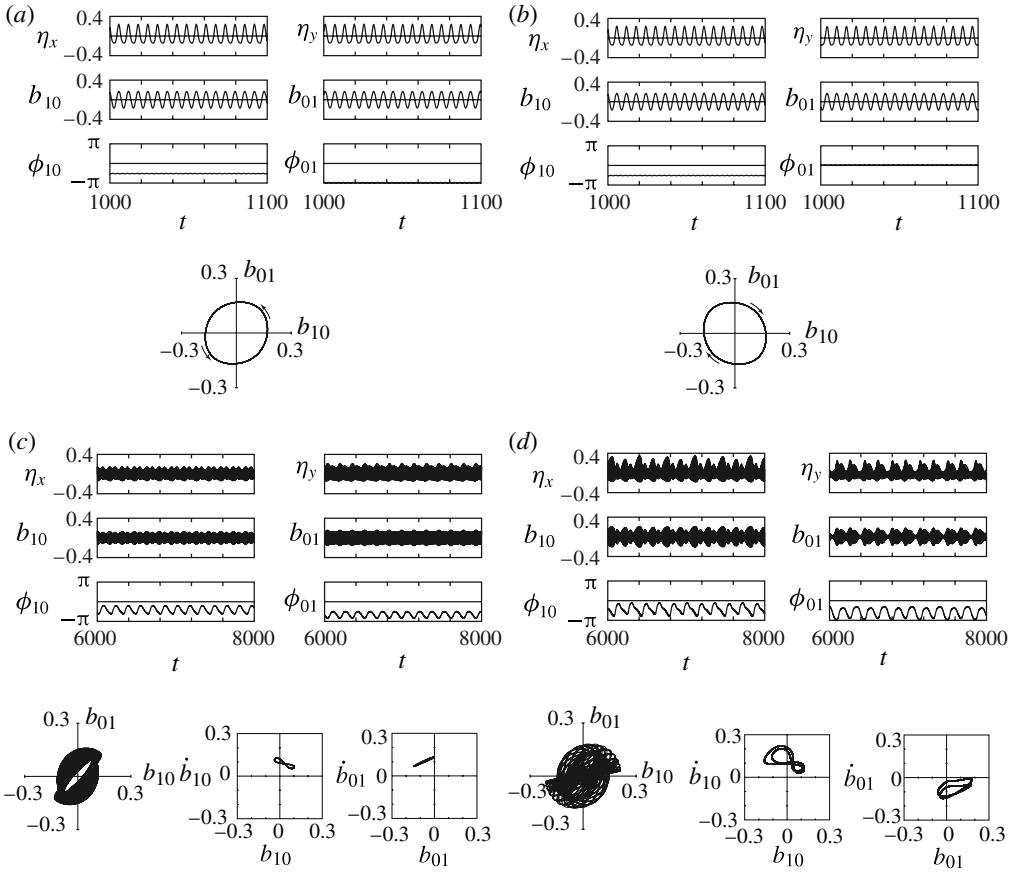

FIGURE 4. For caption see next page.

at the tank walls shown by the symbol '⊗' in figure 1 and are calculated using (2.11*b*) and (2.16). The coordinates of '⊗' are located above the x- and y-axes at $(x, y) = (1/2, 0)$ and $(x, y) = (0, w/2)$. Although η_x includes the components of (1, 0) and higher modes, η_x is almost the same as b_{10} because the nodal line of sloshing mode (1, 0) coincides with the y-axis. The same is true for η_y in terms of (0, 1) mode. The time histories of the phase angles ϕ_{10} and ϕ_{01} are also shown in figure 4. The time history of ϕ_{10} (or ϕ_{01}) can be calculated using the instant values of b_{10} and $\dot{b}_{10}$ (or b_{01} and $\dot{b}_{01}$) during the numerical integration of (2.16) as follows:

$$\left.\begin{aligned} \phi_{10} &= \tan^{-1}\left\{\frac{-b_{10}\sin\omega t - (\dot{b}_{10}/\omega)\cos\omega t}{b_{10}\cos\omega t - (\dot{b}_{10}/\omega)\sin\omega t}\right\}, \\ \phi_{01} &= \tan^{-1}\left\{\frac{-b_{01}\sin\omega t - (\dot{b}_{01}/\omega)\cos\omega t}{b_{01}\cos\omega t - (\dot{b}_{01}/\omega)\sin\omega t}\right\}. \end{aligned}\right\} \tag{3.1}$$

Because the orders of the higher-frequency components included in b_{10} and $\dot{b}_{10}$ are negligible, (3.1) is a reasonable approximation. Lissajous curves are also shown on the (b_{10}, b_{01}) plane to examine the motion of the liquid surface. Figures 4(*a*) and

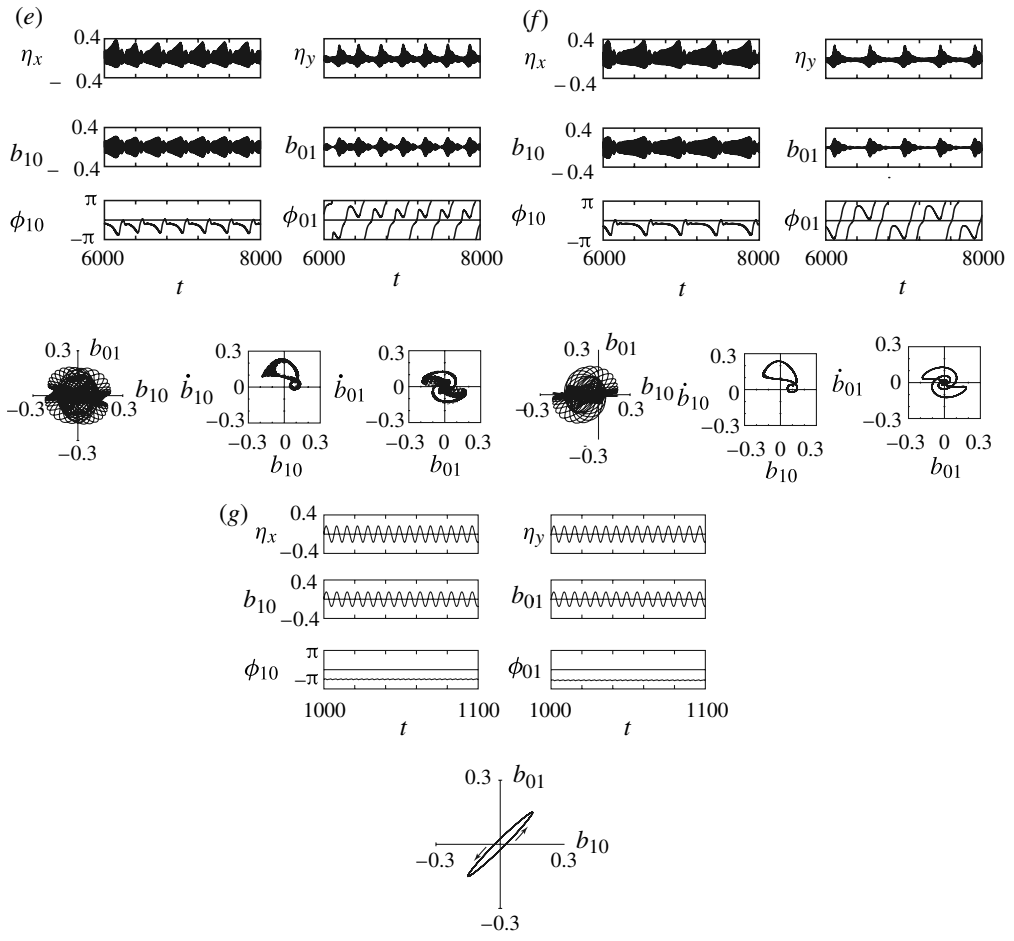

FIGURE 4. (cntd). Stationary time histories of the liquid surface elevations η_x and η_y, modal amplitudes b_{10} and b_{01}, phase angles ϕ_{10} and ϕ_{01}, orbits of the liquid surface (Lissajous curves), and Poincaré maps for figures 3(*a*) and 3(*b*): (*a*) counterclockwise swirl at $\omega = 1.02$; (*b*) clockwise swirl at $\omega = 1.02$; (*c*) AMMs at $\omega = 0.975$; (*d*) AMMs at $\omega = 0.963$; (*e*) chaotic vibrations at $\omega = 0.953$; (*f*) AMMs at $\omega = 0.950$; (*g*) nearly diagonal mode at $\omega = 0.930$.

4(*b*) show the time histories at $\omega = 1.02$ when the initial conditions are chosen from branches H_2F_2 and $H_2'F_2'$ of figures 3(*a*) and 3(*b*), respectively. The amplitudes of b_{10} and b_{01} are constant. However, the phase angles ϕ_{10} and ϕ_{01} fluctuate slightly, because higher-frequency components are included in b_{10} and $\dot{b}_{10}$ (or b_{01} and $\dot{b}_{01}$). $\phi_{10} \cong -\pi/2$ and $\phi_{01} \cong -\pi$ in figure 4(*a*), whereas $\phi_{10} \cong -\pi/2$ and $\phi_{01} \cong 0$ in figure 4(*b*). It is also found from the Lissajous curves that the liquid surface swirls counterclockwise in figure 4(*a*) but clockwise in figure 4(*b*). Figure 4(*c–f*) show the time histories, orbits and Poincaré maps of the AMMs at $\omega = 0.975, 0.963, 0.953$ and 0.950 on branches G_iH_i of figures 3(*a*) and 3(*b*). The orbits in figure 4(*c–f*) are drawn for the time interval $t = 6000$–6500. Poincaré maps are plotted on the $(b_{10}, \dot{b}_{10})$ and $(b_{01}, \dot{b}_{01})$ planes for sufficiently long periods of time. The time histories of the phase angle ϕ_{10} are modulated between zero and $-\pi$ in figure 4(*c–f*). On the other hand, the

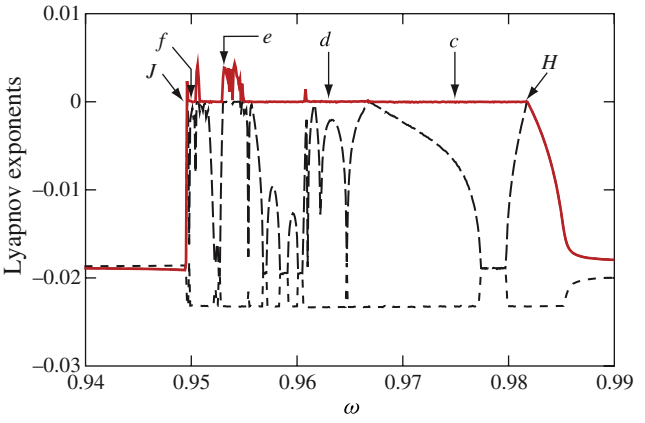

FIGURE 5. (Colour online) Lyapunov exponents corresponding to figure 3(*a*). —— Largest, – – – 2nd largest, and - - - - 3rd largest.

time histories of the phase angle ϕ_{01} are modulated between zero and $-\pi$ in figures 4(*c*) and 4(*d*) but change from $-\pi$ to π in figures 4(*e*) and 4(*f*). It should also be noted that the envelopes of b_{10} and b_{01} and their phase angles change periodically in figure 4(*c*,*d*,*f*), whereas they change irregularly in figure 4(*e*) and are thus chaotic. As the excitation frequency decreases, Poincaré maps exhibit a single-loop (i.e. period-one modulation) in figure 4(*c*), then a double-loop (i.e. period-two modulation) in figure 4(*d*), then chaotic attractors in figure 4(*e*), and finally complicated loops in figure 4(*f*). Figure 4(*g*) shows the time histories at $\omega = 0.930$ for branches E_iG_i. The amplitudes and phase angles of b_{10} and b_{01} are slightly different from each other. It is found from the Lissajous curve that the liquid surface swirls counterclockwise. Compared with figure 4(*a*), the Lissajous curve shape is almost a straight line at 45° from the b_{10}-axis in figure 4(*g*). This implies that the nodal line of sloshing is located close to the diagonal line of the tank cross-section. Here, this type of sloshing is referred to as the 'diagonal mode'.

Figure 5 shows the three largest Lyapunov exponents which are calculated using the method of Wolf *et al.* (1985). The calculation is conducted in such a way that the excitation frequency gradually decreases from $\omega = 1.0$ along branches $F_iH_iG_iE_i$ in figures 3(*a*) and 3(*b*). The positions marked '*c*'–'*f*' correspond to the excitation frequencies in figure 4(*c*–*f*), respectively. Point '*H*' represents a Hopf bifurcation point, after which periodic AMMs appear at points '*c*', '*d*' and '*f*' where the largest Lyapunov exponent at each point is zero. The largest Lyapunov exponent is positive at point '*e*,' so it proves that a chaotic motion appears in figure 4(*e*). As the excitation frequency decreases, a jump phenomenon occurs at point '*J*' where the amplitude jumps from AMMs to stable branches A_iQ_i; thus the largest Lyapunov exponent becomes negative after point '*J*'.

Figure 6 shows a sequence of three-dimensional distribution charts of the maximum liquid surface elevations η_{max} for $\omega = 1.02, 0.963, 0.953$ and 0.930. The purpose of this sequence is to assess the risk of liquid overspill. The values of the parameters are the same as in figure 3(*a*). Figure 6(*a*) corresponds to the case of figure 4(*a*) at $\omega = 1.02$. Even though the amplitudes of b_{10} and b_{01} are comparatively large, η_{max} is comparatively low because there is a phase difference of about $\pi/2$ between b_{10} and b_{01}. Thus the risk of liquid overspill is low. Figures 6(*b*) and 6(*c*) correspond to the

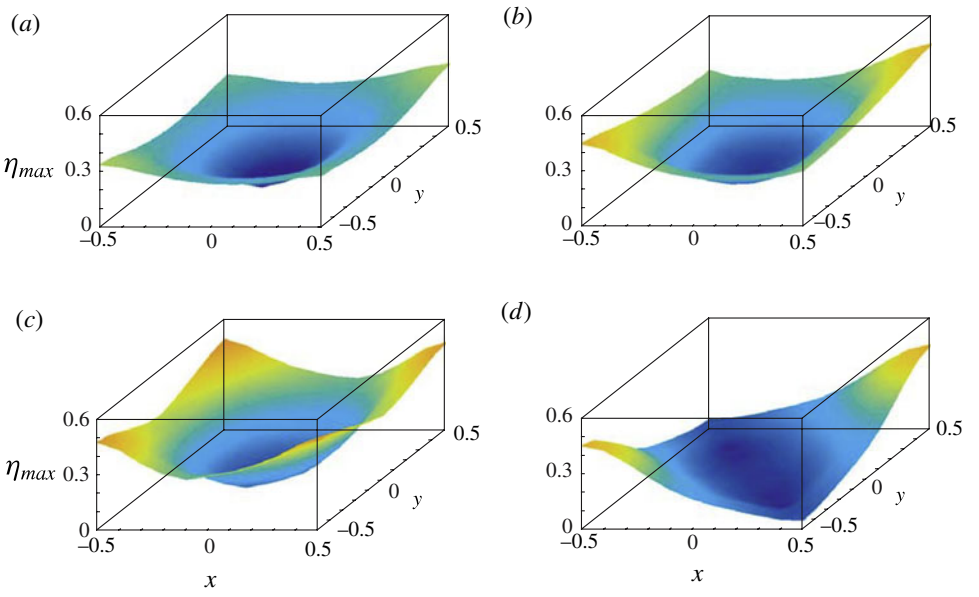

FIGURE 6. (Colour online) Distribution charts of the maximum liquid surface elevation η_{max} for figure 3(*a*): (*a*) $\omega = 1.02$; (*b*) $\omega = 0.963$; (*c*) $\omega = 0.953$; and (*d*) $\omega = 0.930$.

cases of periodic and chaotic AMMs as shown in figures 4(*d*) and 4(*e*), respectively. The liquid elevations in figure 6(*c*) are higher at the corners of the tank than those in figure 6(*b*). Figure 6(*d*) corresponds to the case of figure 4(*g*) and the liquid elevations become significantly large at two opposite corners because b_{10} and b_{01} oscillate in phase. From these charts, chaotic motions in figure 6(*c*) increase the risk of overspill at all four tank corners, while the diagonal mode in figure 6(*d*) increases it at two opposite corners.

3.2. *Influence of the excitation direction*

In real systems, liquid tanks are not always excited in a definite, horizontal direction. Therefore, it is important to investigate the influence of the excitation direction on nonlinear liquid sloshing. Figures 7(*a*)–7(*c*) show the amplitude–frequency response curves for different values of the excitation direction, $\alpha = 5°, 30°$ and $45°$. The values of the other parameters are the same as in figure 3(*a*). Note that when $\alpha \neq 0°$, the tank is subjected to both $a\cos\alpha\cos\omega t$ and $a\sin\alpha\cos\omega t$ in the x- and y-directions, respectively. Therefore, (1, 0) and (0, 1) modes are not only coupled autoparametrically, but also are both directly excited by the external excitation.

Figure 7(*a*) shows the amplitude response curves for $\alpha = 5°$. The amplitudes at points A_2, B_2, C_2, D_2, P_2 and Q_2 are not zero, because (0, 1) mode is also directly excited by $a\sin\alpha\cos\omega t$. A new loop-branch $P_2B_2e_2f_2P_2$ emerges apart from branch $A_2Q_2E_2F_2C_2D_2$. Points B_i and C_i are saddle-node bifurcation points as opposed to the pitchfork bifurcation points in figure 3(*a*). Although vertical thin lines for the AMMs are drawn only for the branches G_iH_i, AMMs also appear at intervals g_ih_i. Figure 7(*b*) shows the amplitude response curves for $\alpha = 30°$. As the value of α increases, points P_i shift to the right and in contrast, points E_i shift to the left. Because points F_i and f_i, appear at nearly the same excitation frequencies, the lengths of branches P_if_i

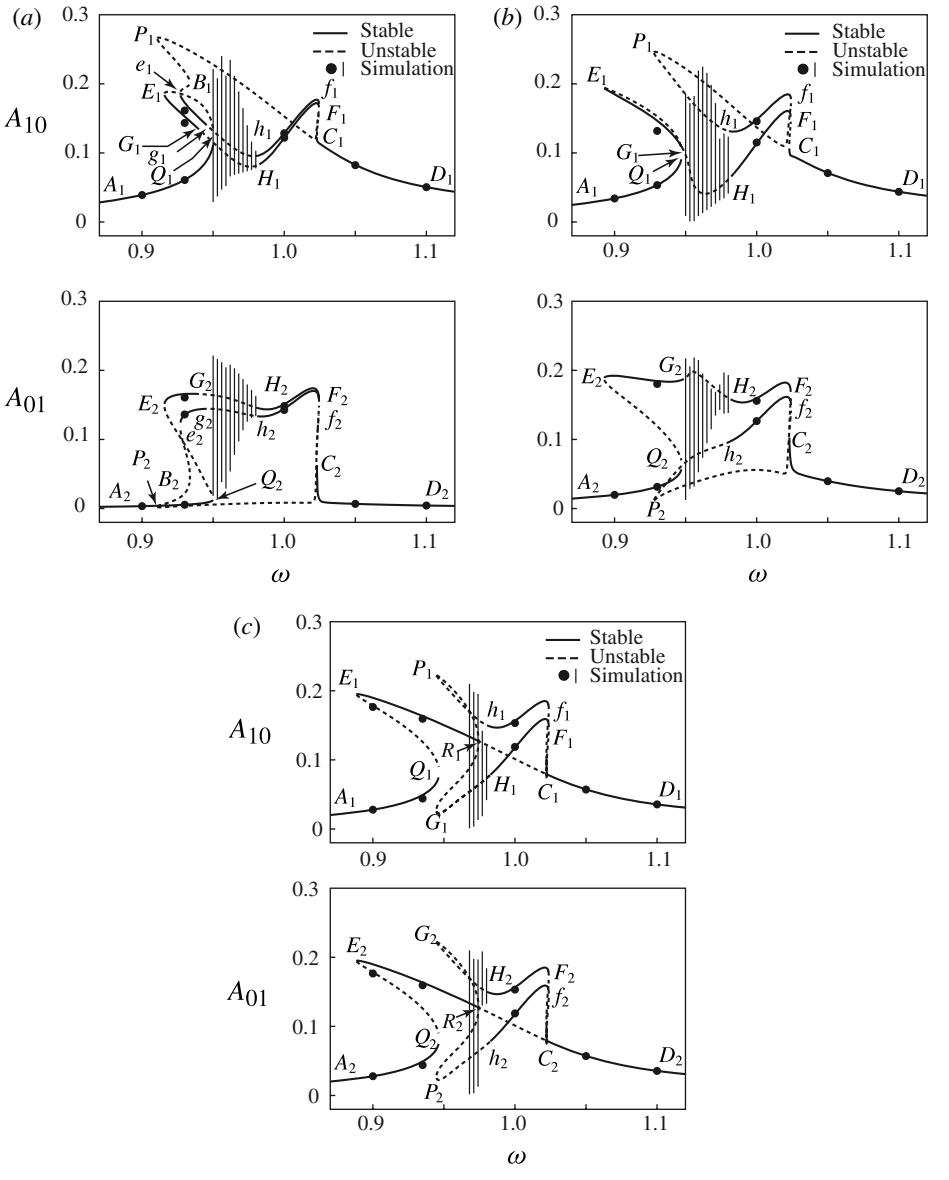

FIGURE 7. Amplitude–frequency response curves of sloshing modes (1, 0) and (0, 1) for $h = 0.6$, $w = 1.0$, $a = 0.0075$, and $\zeta_{ij} = 0.013$: (*a*) $\alpha = 5°$; (*b*) $\alpha = 30°$; and (*c*) $\alpha = 45°$.

shorten, whereas the lengths of branches E_iF_i elongate. Saddle-node bifurcation points B_i and points e_i do not appear. When $\alpha = 45°$ in figure 7(*c*), the shapes of the amplitude response curves of (1, 0) and (0, 1) modes are identical, because they are both excited equally by $a\cos\omega t/\sqrt{2}$. However, branch $G_1H_1F_1C_1$ for A_{10} corresponds to branch $G_2H_2F_2C_2$ for A_{01} and therefore (1, 0) and (0, 1) modes oscillate at different amplitudes. R_iC_i are unstable branches with pitchfork bifurcation points R_i and C_i. From these points, branches $R_iG_iH_iF_iC_i$ and $R_iP_ih_if_iC_i$ emerge and the autoparametric interaction occurs in branches R_iC_i. AMMs appear near points H_i on branches G_iH_i, but they do not appear near points G_i because the amplitudes jump to the stable

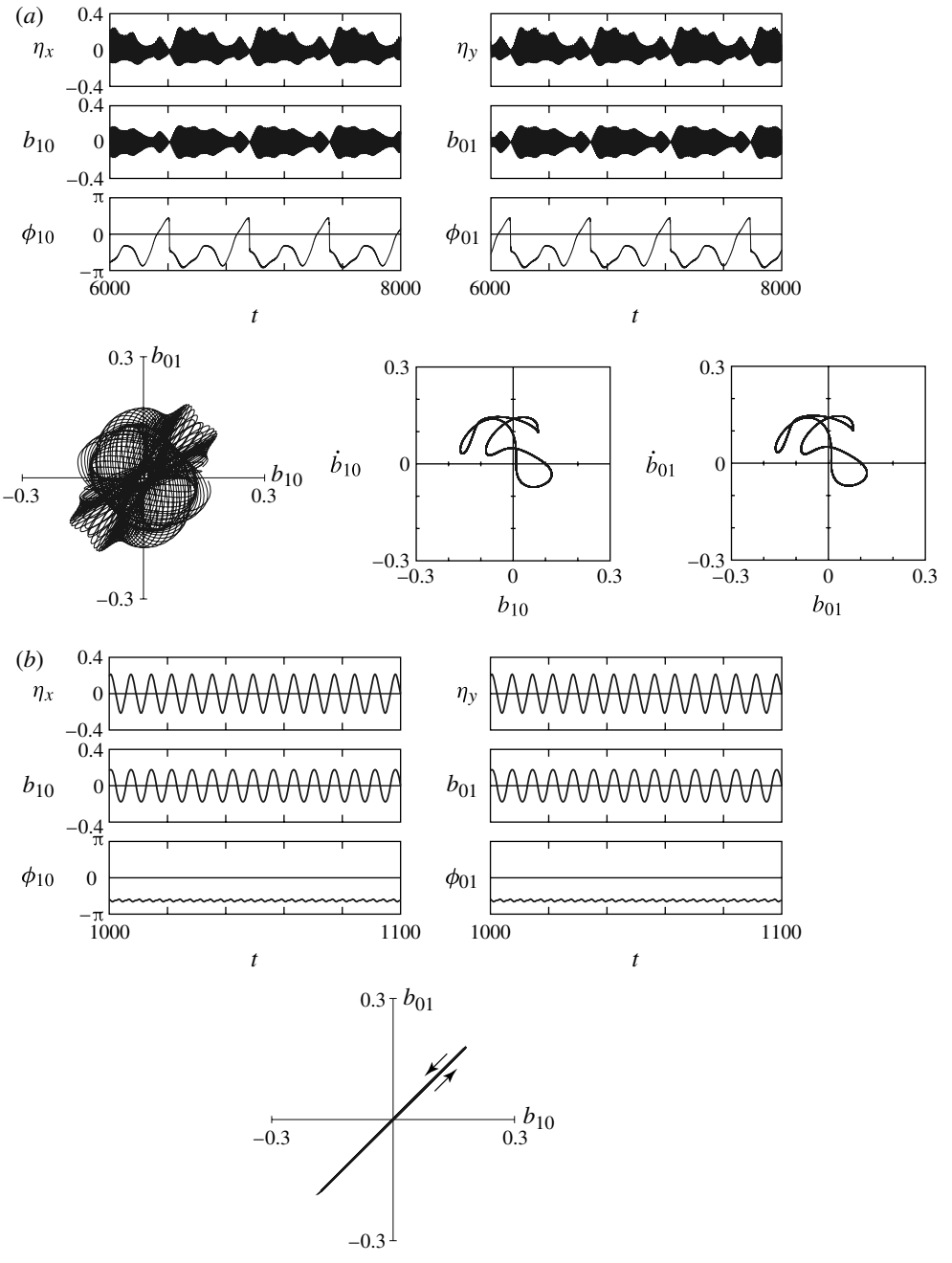

FIGURE 8. Stationary time histories of the liquid surface elevations η_x and η_y, modal amplitudes b_{10} and b_{01}, phase angles ϕ_{10} and ϕ_{01}, orbits of the liquid surface (Lissajous curves), and Poincaré maps for figure 7(*c*): (*a*) AMMs at $\omega = 0.970$; (*b*) diagonal mode at $\omega = 0.900$.

branches E_iR_i. When $45° < \alpha < 90°$, the response curves of (1, 0) and (0, 1) modes are inverted. For example, for $\alpha = 60°$, the frequency response curves for the (1, 0) and (0, 1) modes are the same as those for (0, 1) and (1, 0) modes for $\alpha = 30°$,

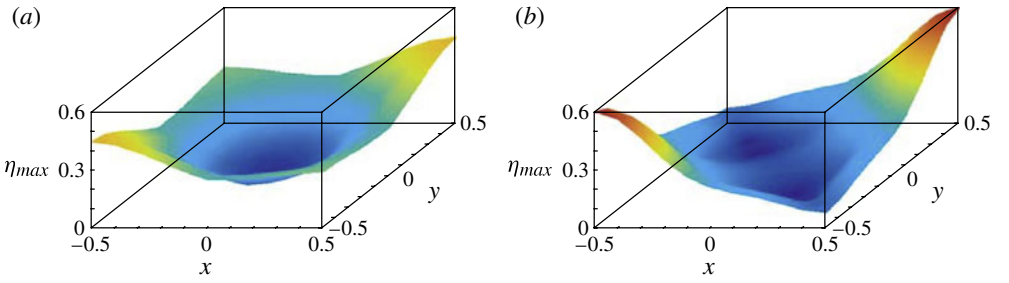

FIGURE 9. (Colour online) Distribution charts of the maximum liquid surface elevation η_{max} for figure 7(*c*): (*a*) $\omega = 0.970$; (*b*) $\omega = 0.900$.

respectively. When α exceeds 90°, the response curves of (1, 0) and (0, 1) modes are identical to the corresponding response curves for $0° < \alpha < 90°$, respectively.

In order to understand the results of figure 7(*c*) in more detail, the corresponding time histories are shown in figure 8. The time histories in figure 8(*a*) exhibit periodic AMMs in both amplitudes and phase angles of (1, 0) and (0, 1) modes at $\omega = 0.97$. Poincaré maps on the $(b_{10}, \dot{b}_{10})$ and $(b_{01}, \dot{b}_{01})$ planes exhibit complicated loops, and the envelopes of the time histories of b_{10} and b_{01} are periodic. Although the shapes of these two loops are identical, the individual points are not. At $\omega = 0.90$ in figure 8(*b*), the time histories of (1, 0) and (0, 1) modes are identical, and therefore the Lissajous curve is a straight line inclined at 45° to the b_{10}-axis. This implies that the nodal line of liquid sloshing coincides with the diagonal line of the tank cross-section and the diagonal mode occurs.

Figures 9(*a*) and 9(*b*) show the three-dimensional distribution charts of the maximum liquid surface elevations η_{max} at $\omega = 0.97$ and 0.90 corresponding to figures 8(*a*) and 8(*b*), respectively. Figure 9(*a*) is similar to figure 6(*b*), and AMMs appear. In figure 9(*b*), the distribution of η_{max} is both steeper and higher near the two opposite corners compared with figure 6(*d*), and the risk of overspill becomes higher.

Bifurcation sets are calculated using the software AUTO (Doedel *et al.* 1997) to examine the influence of the excitation direction in more detail. Figure 10 shows the bifurcation sets on the (ω, α) plane, when the values of the system parameters are the same as in figure 3(*a*). Each bifurcation set is named corresponding to the bifurcation point which occurs in the frequency response curves. The solid and broken lines represent saddle-node and Hopf bifurcation sets, respectively. The four cases presented in figures 3(*a*) and 7(*a–c*) are included so that their system behaviours can be easily compared and evaluated. The positions of saddle-node bifurcation sets '*F*', '*f*' and '*Q*' as well as Hopf bifurcation sets '*H*' and '*h*' are almost independent of the value of α. As α increases, saddle-node bifurcation sets '*P*' and '*E*' shift to the right and left, respectively, thus the range '*Pf*' decreases while the range '*EF*' increases. Point '*E*' at $\alpha = 0°$ bifurcates to sets '*E*' and '*e*', and point *G* at $\alpha = 0°$ bifurcates to sets '*G*' and '*g*'. Set '*e*' encounters set '*B*' near $\alpha = 12°$ and then disappears. Set '*B*' connects with set '*g*' near $\alpha = 16°$ and then they both disappear. Hopf bifurcation set '*G*' bifurcates near $\alpha = 33°$ to sets '*G*' and '*R*'. Saddle-node sets '*R*' and '*C*' change to pitchfork bifurcation points at $\alpha = 45°$. As previously mentioned, the autoparametric interaction emerges from points '*B*' and '*C*' at $\alpha = 0°$, whereas it emerges from points '*R*' and '*C*' at $\alpha = 45°$. Additionally, 45° acts as an axis of symmetry for the bifurcation sets, thus all sets appear as a mirror image for values 45° to 90°. Furthermore all bifurcation sets for $0° < \alpha < 90°$ repeat every 90°.

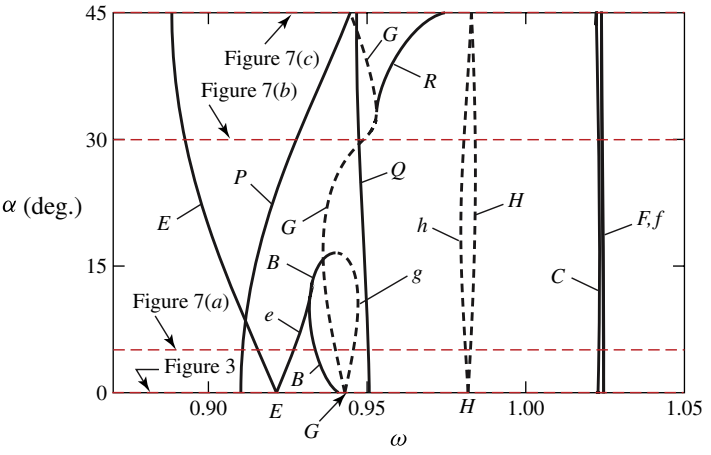

FIGURE 10. (Colour online) Bifurcation sets on the (ω, α) plane when $h = 0.6$, $w = 1.0$ and $a = 0.0075$, including the cases of figures 3 and 7(*a–c*). —— Saddle-node bifurcation set; — — — Hopf bifurcation set.

3.3. *Influence of the aspect ratio of the tank cross-section*

In §§ 3.1 and 3.2, the tank has a square cross-section, and hence the natural frequencies of (1, 0) and (0, 1) modes equal 1.0. In this section, the influence of the aspect ratio of the tank cross-section is examined to investigate the effect of the imperfections in the manufacturing process of square tanks.

Figures 11(*a*) and 11(*b*) show the amplitude–frequency response curves when the values of the system parameters are the same as in figure 3(*a*) including $\alpha = 0°$, except for w. In figure 11(*a*), w is decreased from 1.0 to 0.95, and the natural frequencies of sloshing modes are $p_{10} = 1.0$ and $p_{01} = 1.030$. Compared with figure 3(*a*), Hopf bifurcation points G_i and H_i do not appear. The excitation frequency range at which the autoparametric interaction occurs increases because p_{01} changes from 1.0 to 1.030 and points C_i shift to the right. When w is decreased, pitchfork bifurcation points B_i gradually approach and eventually meet points P_i. Points E_i also shift to the left, hence branches E_iF_i become longer than those in figure 3(*a*). Figure 11(*b*) shows the amplitude response curves when the value of w is increased to 1.05. The natural frequencies of sloshing are $p_{10} = 1.0$ and $p_{01} = 0.972$. Pitchfork bifurcation points B_i approach points Q_i, and points C_i shift to the left. Therefore, the excitation frequency range of the autoparametric interaction shrinks, compared with figure 3(*a*). Hopf bifurcation points do not appear. Figures 11(*c*) and 11(*d*) show the influence of the tank aspect ratio on the frequency response curves when $\alpha = 45°$ and the same parameters as figure 7(*c*). In figure 11(*c*), the tank breadth w is slightly increased to 1.001, therefore the tank is no longer a perfect square. The natural frequencies of sloshing are $p_{10} = 1.0$ and $p_{01} = 0.999$. Pitchfork bifurcation points R_i and C_i in figure 7(*c*) become saddle-node bifurcation points. Furthermore, saddle-node bifurcation points R_i are followed by a perturbed pitchfork bifurcation. Branches $P_ih_if_iP_i$ form closed loops and are isolated from all other branches. In figure 11(*d*), when w is further increased to 1.05, loop-branches $P_ih_if_iP_i$ shrink. Because saddle-node bifurcation points R_i do not appear and Hopf bifurcation points G_i shift to the left, AMMs appear on G_iH_i over a wider excitation frequency range than the cases of figures 7(*c*) and 11(*c*). Compared to figure 11(*b*), which has the same values of the

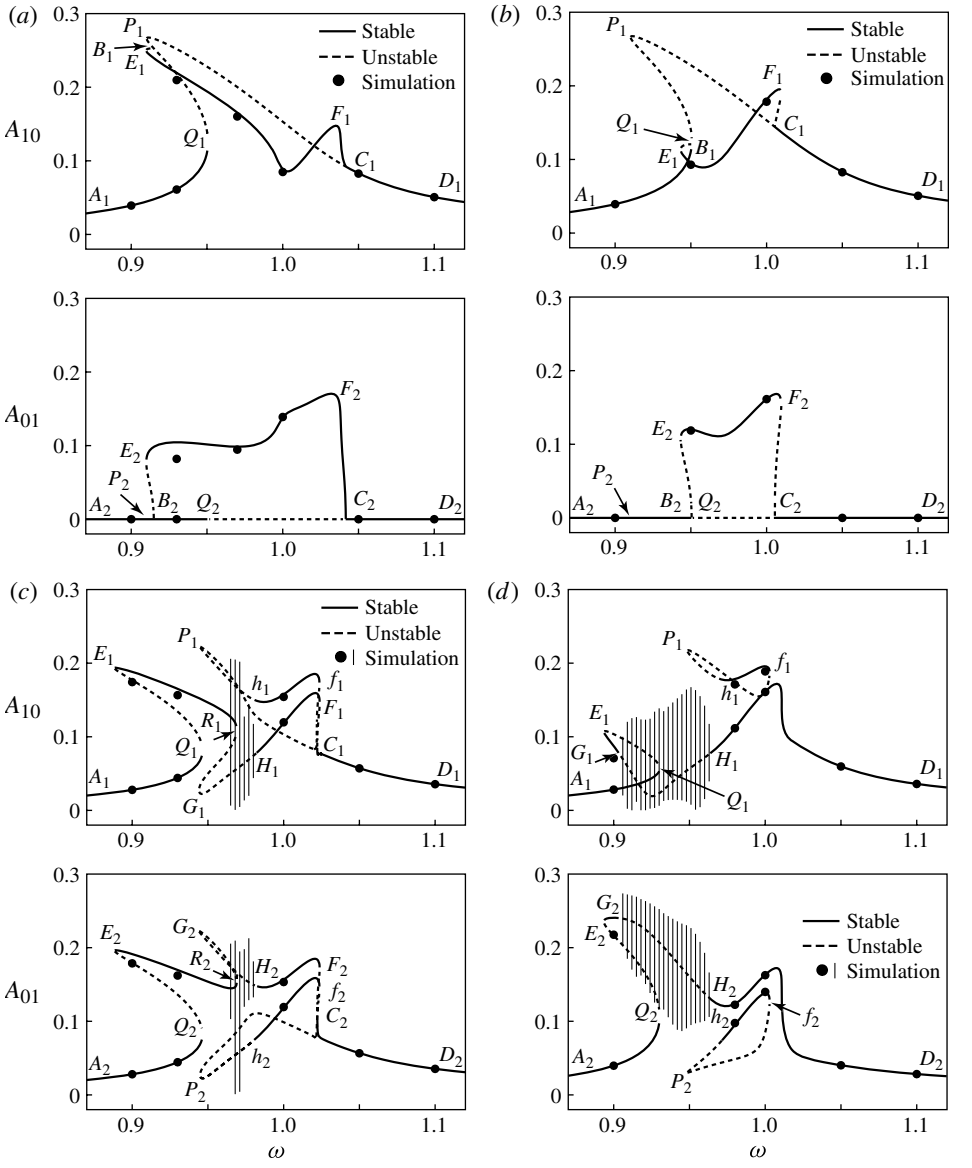

FIGURE 11. Amplitude–frequency response curves for sloshing modes (1, 0) and (0, 1) for $h = 0.6$, $\zeta_{ij} = 0.013$, $a = 0.0075$, and different tank breadths and excitation directions: (*a*) $w = 0.95$ and $\alpha = 0°$ ($p_{10} = 1.0, p_{01} = 1.030$); (*b*) $w = 1.05$ and $\alpha = 0°$ ($p_{10} = 1.0, p_{01} = 0.972$); (*c*) $w = 1.001$ and $\alpha = 45°$ ($p_{10} = 1.0, p_{01} = 0.999$); (*d*) $w = 1.05$ and $\alpha = 45°$ ($p_{10} = 1.0, p_{01} = 0.972$).

system parameters but different excitation direction, it can be seen that a change in α has a greater influence on the response curves of the system than a change in w.

The influence of the liquid level on the amplitude–frequency response curves was also investigated, and the results agreed with those previously reported (Ibrahim 2005; Faltinsen & Timokha 2009). It was confirmed that there is a critical liquid depth at which the response curves for liquid sloshing switch from soft- to hard-spring types.

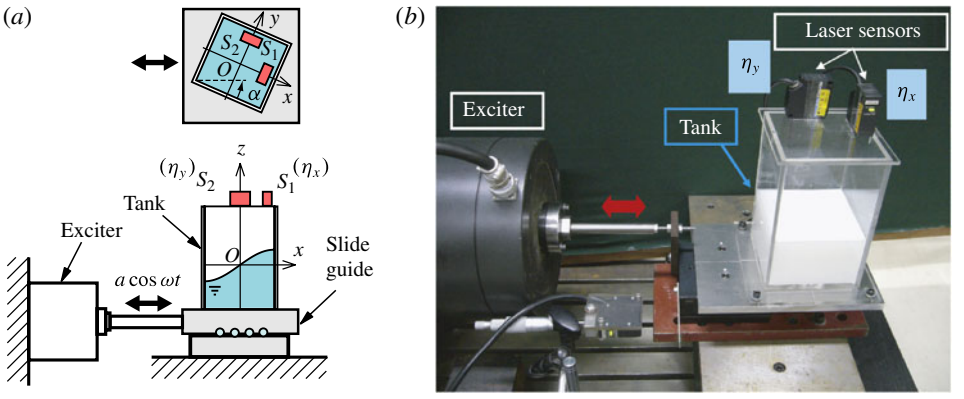

FIGURE 12. (Colour online) Experimental setup: (*a*) schematic diagram; (*b*) photo.

4. Experimental results

A series of experiments were conducted with the purpose of validating the theoretical results. Figure 12(*a*) shows a schematic diagram of the experimental apparatus, and its photo is shown in figure 12(*b*). A square tank was mounted on the slide guide which was horizontally driven in one direction by sinusoidal excitation with a constant amplitude using an electromagnetic exciter and its controller. The excitation angle α was adjustable by rotating the tank. The dimensions of the tank were $h = 60$ mm, $l = 100$ mm and $w = 100$ mm. Curve fitting was used to match the theoretical results to the experimental data, thus identifying the damping ratios $\zeta_{ij} = 0.015$. These ratios were similar both to the measured value of $\zeta_{10} = 0.0128$ obtained by the logarithmic decrement and the theoretical values based on Keulegan theory (Faltinsen *et al.* 2006*b*; Faltinsen & Timokha 2009) calculated as $\zeta_{10} = \zeta_{01} = 0.0138$, $\zeta_{20} = \zeta_{02} = 0.0167$ and $\zeta_{30} = \zeta_{03} = 0.0185$. Because the damping ratios of higher modes are about the same as the predominant mode, $\zeta_{ij} = 0.015$ are used for all modes. Tap water with a small amount of white watercolour was used as a test liquid. Excitation amplitudes of the exciter head were slightly different depending on the following three experimental conditions as shown in figures 13, 15(*a*) and 15(*b*). Laser sensors S_1 and S_2 were set above the x- and y-axes, namely the nodal lines of (0, 1) and (1, 0) sloshing modes, to detect the liquid elevations η_x and η_y at positions $(x, y) = (40\text{ mm}, 0)$ and (0, 40 mm), respectively. The measured natural frequencies p_{10} and p_{01} of sloshing were both 2.730 Hz which was nearly identical to the theoretical value given by (2.5).

Figure 13 shows the comparison between the amplitude response curves of the experimental and theoretical results for η_x and η_y, respectively, when $a = 0.727$ mm and $\alpha = 0°$. The corresponding analytical amplitudes A_{10} and A_{01} for (1, 0) and (0, 1) sloshing modes are plotted, respectively. They are drawn in solid and broken lines which are calculated by (2.18) and (2.20). Symbol ◯ represents the experimental data with constant amplitude. Symbols ◐ and ◑ represent counterclockwise and clockwise swirl motions, respectively. Red circles represent the experimental data of the maximum modulated amplitude when AMMs appeared. As the excitation frequency $f[=\omega/(2\pi)]$ was increased from 2.40 Hz, a jump phenomenon occurred at $f = 2.63$ Hz. AMMs then appeared at the excitation frequency range corresponding to branches G_iH_i. Counterclockwise or clockwise swirl motions were observed

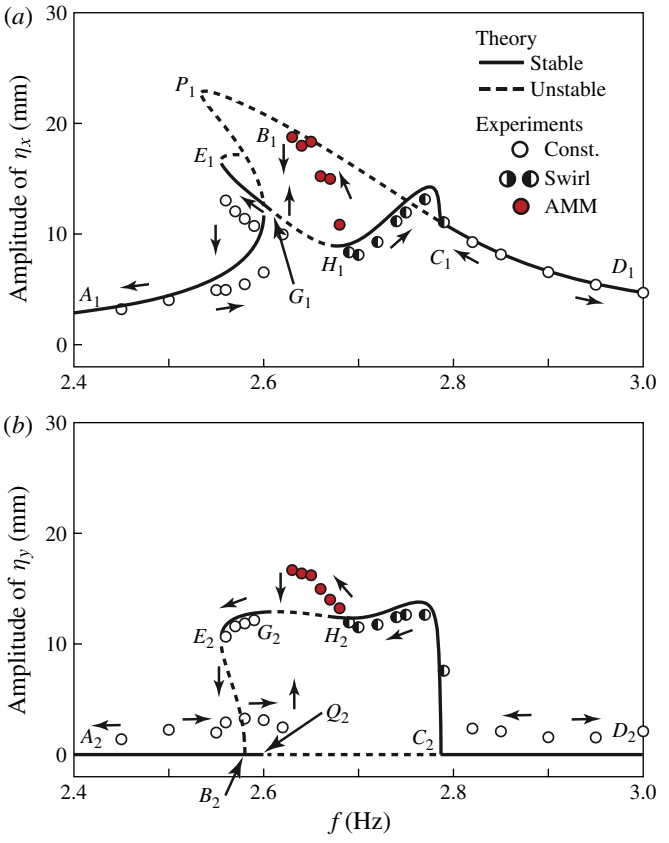

FIGURE 13. (Colour online) Measured and predicted amplitude–frequency responses of liquid free surface at the positions of sensors S_1 and S_2, as shown in figure 12(*a*), for $h = 60$ mm, $l = 100$ mm, $w = 100$ mm, $\zeta_{ij} = 0.015$, $a = 0.727$ mm and $\alpha = 0°$.

during 2.69–2.79 Hz depending on the initial conditions. When f was decreased from 3.00 Hz, the experimental data corresponding to branches G_iE_i were observed. It is found that the theoretical results were qualitatively in good agreement with the experimental data.

Figure 14 shows the stationary time histories of η_x and η_y measured at the discrete excitation frequencies, $f = 2.77, 2.65, 2.63$ and 2.58 Hz in figure 13. Figures 14(*a*) and 14(*b*) show constant amplitudes at $f = 2.77$ Hz; in which the former exhibits a counterclockwise swirl and the latter, a clockwise swirl. These are similar to the results predicted in figures 4(*a*) and 4(*b*). AMMs with periodic envelopes appeared at $f = 2.65$ Hz in figure 14(*c*), and their wave forms are similar to those in figure 4(*d*). Chaotic motions with irregular envelopes appeared at $f = 2.63$ Hz in figure 14(*d*), and their wave forms are similar to those in figure 4(*e*). Sloshing with constant amplitudes was observed at $f = 2.58$ Hz in figure 14(*e*) and it was found that the time histories of η_x and η_y are in phase; hence the liquid surface oscillated on both sides of the diagonal line of the tank cross-section. This phenomenon, the diagonal mode, was also predicted in figure 4(*g*).

Figure 15(*a*) shows the comparison between the experimental and theoretical results, when $a = 0.726$ mm and $\alpha = 30°$. When f was increased from 2.40 Hz,

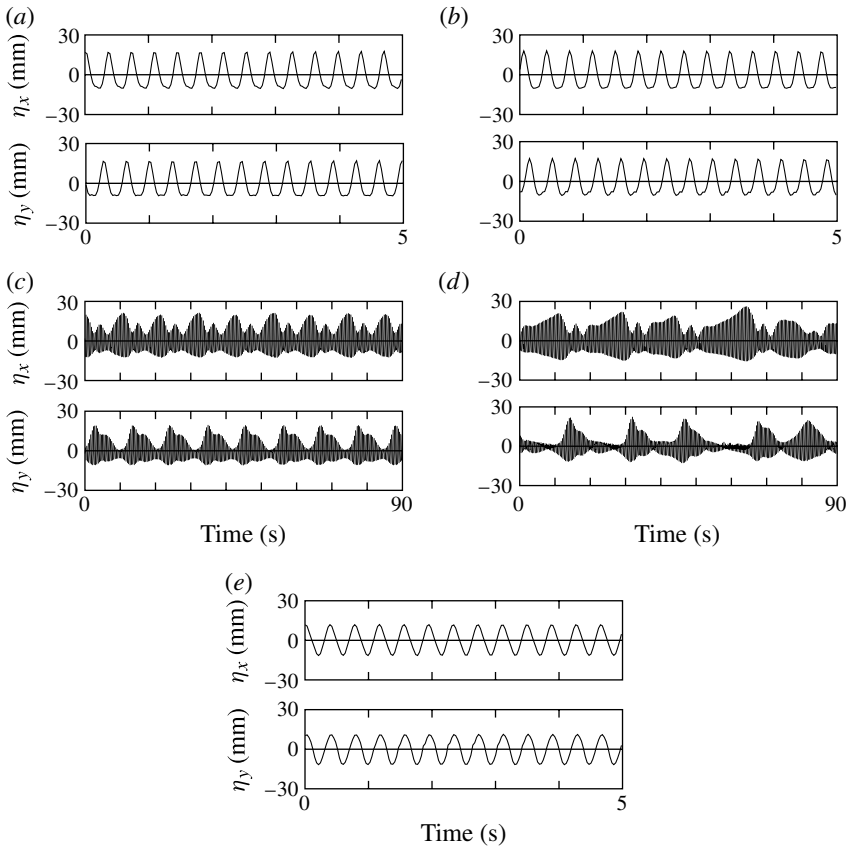

FIGURE 14. Stationary time histories of η_x and η_y measured at the different values of excitation frequencies in figure 13: (*a*) counterclockwise swirl at $f = 2.77$ Hz; (*b*) clockwise swirl at $f = 2.77$ Hz; (*c*) AMMs at $f = 2.65$ Hz; (*d*) chaotic surface oscillations at $f = 2.63$ Hz; and (*e*) diagonal mode at $f = 2.58$ Hz.

a jump phenomenon occurred at $f = 2.63$ Hz. AMMs appeared in the range of $f = 2.63$–2.70 Hz which corresponds to the intervals G_iH_i. When f increased further, swirling waves were observed depending on the initial condition in the range of $f = 2.71$–2.80 Hz. When f decreased from 3.00 Hz, the experimental data corresponding to branches G_iE_i were observed. These experimental results were predicted in figure 7(*b*). Figure 15(*b*) shows the comparison between the experimental and theoretical results when $a = 0.717$ mm and $\alpha = 45°$. When f was increased from 2.40 Hz, a jump phenomenon occurred at $f = 2.63$ Hz and (1, 0) and (0, 1) modes appeared at almost the same amplitudes corresponding to branches E_iR_i. When f was increased further, AMMs appeared for $f = 2.66$–2.69 Hz, shown by the symbol ● in the interval P_ih_i. Constant amplitudes were observed corresponding to branches h_iC_i and the liquid surface swirled clockwise. When f was decreased from $f = 3.00$ Hz, experimental data were recorded corresponding to branches C_iH_i and the liquid surface swirled counterclockwise. As predicted in figure 7(*c*), it should be noted that two patterns were observed for each predominant mode in experiments; one corresponded to branches C_ih_i, and the other to branches C_iH_i. Thus (1, 0) and (0, 1) modes oscillated at different amplitudes. AMMs appeared again during $f = 2.65$–2.69 Hz.

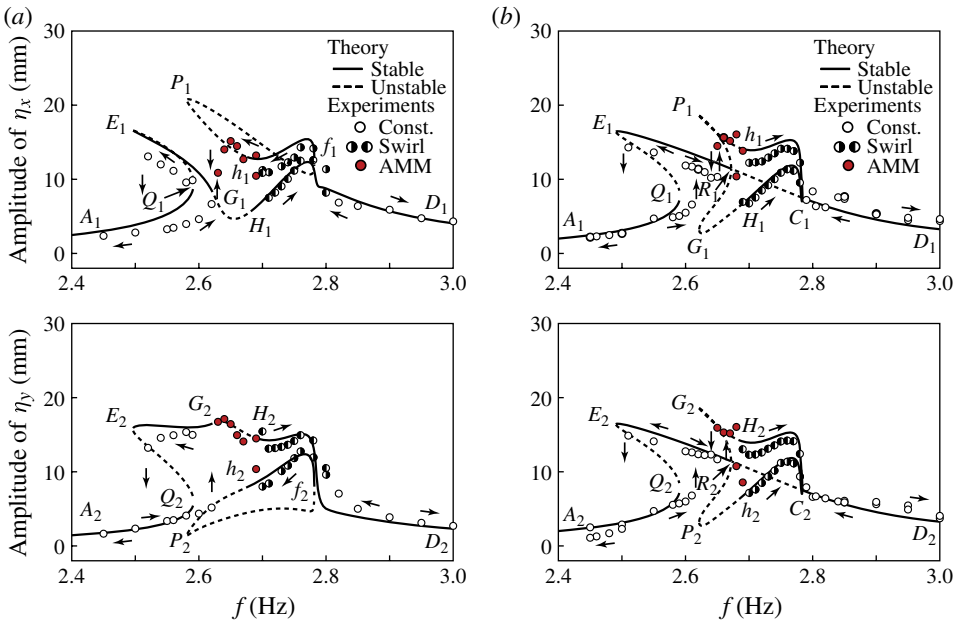

FIGURE 15. (Colour online) Measured and predicted amplitude–frequency responses of liquid free surface for the same parameters as figure 13 but different values of excitation amplitude and direction: (*a*) $a = 0.726$ mm, and $\alpha = 30°$ corresponding to figure 7(*b*); (*b*) $a = 0.717$ mm, and $\alpha = 45°$ corresponding to figure 7(*c*).

When f was decreased further, (1, 0) and (0, 1) modes oscillated in phase at almost the same amplitudes for $f = 2.51$–2.62 Hz which correspond to branches E_iR_i.

It is found that depending on the excitation frequency, planar, clockwise or counterclockwise swirl motions, or sloshing with a nodal line along the diagonal line of the tank cross-section appears. Hopf bifurcations occur, and AMMs including chaotic motions may also appear. According to the comparison between the theoretical results and experimental data for the three experimental conditions mentioned above, the theoretical results quantitatively agreed with the experimental data. Therefore, it can be concluded that the validity of the theoretical analysis was confirmed.

5. Conclusion

In this paper, the dynamic behaviour of nonlinear liquid sloshing in rigid square and nearly square tanks, subjected to obliquely horizontal, sinusoidal excitation, was theoretically and experimentally investigated. Because the theoretical analysis is precise in that the damping effect of sloshing is considered, the theoretical frequency response curves contain both stable and unstable steady-state solutions. These curves for amplitudes and phase angles can clearly explain the phenomena of nonlinear sloshing dynamics in real systems. Furthermore, this method has been applied when investigating the direction of horizontal excitation relative to the tank and has generated novel results. The results of the influence of deviations from a perfect square cross-section were also clearly shown. The detailed results can be summarized as follows.

(*a*) For high liquid levels, when the excitation direction $\alpha = 0°$, only (1, 0) sloshing mode is directly excited. However, (0, 1) sloshing mode can appear in a limited excitation frequency range due to the autoparametric interaction. When both modes appear simultaneously at this range, the following behaviours of liquid sloshing may occur: (i) both modes oscillate in phase at constant amplitudes similar to the 'diagonal mode'; (ii) either clockwise or counterclockwise swirl motion may be observed; and (iii) Hopf bifurcations occur, followed by amplitude-modulated motions including chaotic motions.

(*b*) When $\alpha \neq 0°$, (1, 0) and (0, 1) modes are nonlinearly coupled and both are directly excited. The responses become more complicated than the case of $\alpha = 0°$ and isolated loop-branches appear on the response curves. For the particular case of $\alpha = 45°$, the response curves for (1, 0) and (0, 1) modes have identical shapes, because these modes are excited equally by $a\cos\omega t/\sqrt{2}$. Innovative results are detailed and include a specific excitation frequency range in which two branches are generated on the frequency response curves for either predominant mode and they oscillate at different amplitudes due to the autoparametric interaction. Furthermore, either counterclockwise or clockwise swirl motions were observed in this excitation frequency range depending on the initial conditions.

(*c*) When (1, 0) and (0, 1) modes oscillate in phase along the nodal line of the tank cross-section, the diagonal mode occurs causing high liquid elevations at two opposite corners of the tank. Therefore, the risk of overspill is significantly increased. Furthermore, chaotic motions cause high liquid elevations at all four tank corners, thus overspill risks are increased.

(*d*) Slight deviations of the tank aspect ratio significantly affect the response curves due to the difference between the natural frequencies of (1, 0) and (0, 1) modes. Furthermore, when $\alpha = 45°$, a slight change of the tank aspect ratio causes a perturbed pitchfork bifurcation instead of a pitchfork bifurcation to occur.

(*e*) In experiments, the theoretical results were quantitatively in good agreement with the experimental data. Therefore, the validity of the theoretical analysis was confirmed.

For further works examining nonlinear sloshing behaviour, the aspect ratio of the tank cross-section could be changed so that the natural frequencies of (1, 0) and (0, 1) modes satisfy different internal resonance conditions, such as $p_{10}{:}p_{01} = 1{:}2$ and 1:3. In such cases, similar, different, or more complicated phenomena may occur.

Appendix. The nonlinear terms H_m in (2.16)

$$\left.\begin{aligned}
H_1 &= S_1\dot{b}_{10}\dot{b}_{20} + S_2\dot{b}_{01}\dot{b}_{11} + S_3\dot{b}_{10}^2 b_{10} + S_4\dot{b}_{01}^2 b_{10} + S_5\dot{b}_{10}\dot{b}_{01}b_{01} + S_6 b_{10}b_{20} \\
&\quad + S_7 b_{01}b_{11} + S_8 b_{10}^3 + S_9 b_{01}^2 b_{10}, \\
H_2 &= S_{10}\dot{b}_{01}\dot{b}_{02} + S_{11}\dot{b}_{10}\dot{b}_{11} + S_{12}\dot{b}_{01}^2 b_{01} + S_{13}\dot{b}_{10}^2 b_{01} + S_{14}\dot{b}_{10}\dot{b}_{01}b_{10}, \\
&\quad + S_{15} b_{01}b_{02} + S_{16} b_{10}b_{11} + S_{17} b_{01}^3 + S_{18} b_{10}^2 b_{01} \\
H_3 &= S_{19}\dot{b}_{10}^2 + S_{20}\dot{b}_{10}\dot{b}_{30} + S_{21} b_{10}^2 + S_{22} b_{10}b_{30}, \\
H_4 &= S_{23}\dot{b}_{01}^2 + S_{24}\dot{b}_{01}\dot{b}_{03} + S_{25} b_{01}^2 + S_{26} b_{01}b_{03}, \\
H_5 &= S_{27}\dot{b}_{10}\dot{b}_{20} + S_{28}\dot{b}_{10}^2 b_{10} + S_{29} b_{10}b_{20} + S_{30} b_{10}^3, \\
H_6 &= S_{31}\dot{b}_{01}\dot{b}_{02} + S_{32}\dot{b}_{01}^2 b_{01} + S_{33} b_{01}b_{02} + S_{34} b_{01}^3, \\
H_7 &= S_{35}\dot{b}_{10}\dot{b}_{01} + S_{36} b_{10}b_{01},
\end{aligned}\right\} \quad \text{(A 1)}$$

where the symbols S_n $(n = 1, 2, \ldots, 36)$ are constants defined from the system parameters and their complete expressions are omitted here.

REFERENCES

ABRAMSON, H. N. 1966 The dynamic behavior of liquids in moving contains. *NASA SP*-106.

DOEDEL, E. J., CHAMPNEYS, A. R., FAIRGRIEVE, T. F., KUZNETSOV, Y. A., SANDSTEDE, B. & WANG, X. 1997 Continuation and bifurcation software for ordinary differential equations (with HomCont), AUTO97. Concordia University.

FALTINSEN, O. M., ROGNEBAKKE, O. F., LUKOVSKY, I. A. & TIMOKHA, A. N. 2000 Multidimensional modal analysis of nonlinear sloshing in a rectangular tank with finite water depth. *J. Fluid Mech.* **407**, 201–234.

FALTINSEN, O. M., ROGNEBAKKE, O. F. & TIMOKHA, A. N. 2003 Resonant three-dimensional nonlinear sloshing in a square-base basin. *J. Fluid Mech.* **487**, 1–42.

FALTINSEN, O. M., ROGNEBAKKE, O. F. & TIMOKHA, A. N. 2005 Resonant three-dimensional nonlinear sloshing in a square-base basin. Part 2. Effect of higher modes. *J. Fluid Mech.* **523**, 199–218.

FALTINSEN, O. M., ROGNEBAKKE, O. F. & TIMOKHA, A. N. 2006*a* Resonant three-dimensional nonlinear sloshing in a square-base basin. Part 3. Base ratio perturbations. *J. Fluid Mech.* **551**, 93–116.

FALTINSEN, O. M., ROGNEBAKKE, O. F. & TIMOKHA, A. N. 2006*b* Transient and steady-state amplitudes of resonant three-dimensional sloshing in a square base tank with a finite fluid depth. *Phys. Fluids* **18** (1), 012103.

FALTINSEN, O. M. & TIMOKHA, A. N. 2009 *Sloshing*. Cambridge University Press.

FENG, Z. C. 1997 Transition to travelling waves from standing waves in a rectangular container subjected to horizontal excitations. *Phys. Rev. Lett.* **73** (3), 415–418.

FENG, Z. C. 1998 Coupling between neighbouring two-dimensional modes of water waves. *Phys. Fluids* **10** (9), 2405–2411.

FUNAKOSHI, M. & INOUE, S. 1988 Surface waves due to resonant horizontal oscillation. *J. Fluid Mech.* **192**, 219–247.

HAYAMA, S., ARUGA, K. & WATANABE, T. 1983 Nonlinear response of sloshing in rectangular tanks (1st report, nonlinear response of surface elevation). *Bull. JSME* **26** (219), 1641–1648.

HILL, D. F. 2003 Transient and steady-state amplitudes of forced waves in rectangular basins. *Phys. Fluids* **15** (6), 1576–1587.

HUTTON, R. E. 1963 An investigation of resonant, nonlinear, nonplaner free surface oscillations of a fluid. *NASA Tech. Note* D-1870, 1–64.

IBRAHIM, R. A. 2005 *Liquid Sloshing Dynamics*. Cambridge University Press.

IKEDA, T. 2003 Nonlinear parametric vibrations of an elastic structure with a rectangular liquid tank. *Nonlinear Dyn.* **33** (1), 43–70.

IKEDA, T. & IBRAHIM, R. A. 2008 Nonlinear surface waves in a square liquid tank under obliquely horizontal excitation. In *Proceedings of the 22nd International Congress of Theoretical and Applied Mechanics (ICTAM2008), Adelaide, Australia, August 24–29*. ISBN 978-0-9805142.

IKEDA, T. & NAKAGAWA, N. 1997 Non-linear vibrations of a structure caused by water sloshing in a rectangular tank. *J. Sound Vib.* **201** (1), 23–41.

KIMURA, K., TAKAHARA, H. & OGURA, H. 1996 Three-dimensional sloshing analysis in a rectangular tank subjected to pitching excitation. *Trans. Japan Soc. Mech. Engng* C **62** (596), 1285–1294 (in Japanese).

MILES, J. W. 1984 Resonantly forced surface waves in a circular cylinder. *J. Fluid Mech.* **149**, 15–31.

MOISEEV, N. N. 1958 To the theory of nonlinear oscillations of a limited liquid volume. *Appl. Math. Mech. (PMM)* **22**, 612–621 (in Russian).

ROYON-LEBEAUD, A., HOPFINGER, E. J. & CARTELLIER, A. 2007 Liquid sloshing and wave breaking in circular and square-base cylindrical containers. *J. Fluid Mech.* **577**, 467–494.

STOKER, J. J. 1950 *Nonlinear Vibrations*. John Wiley & Sons.

TAKAHARA, H. & KIMURA, K. 2002 Frequency response of sloshing in a rectangular tank subjected to pitching excitation. *Trans. Japan Soc. Mech. Engng* C **68** (667), 738–746 (in Japanese).

WOLF, A., SWIFT, J. B., SWINNEY, H. L. & VASTANO, J. A. 1985 Determining Lyapunov exponents from a time series. *Physica* D **16**, 285–317.

YOSHIMATSU, K. & FUNAKOSHI, M. 2001 Surface waves in a square container due to resonant horizontal oscillations. *J. Phys. Soc. Japan* **70** (2), 394–406.